

Intergalactic Dust Extinction in Hydrodynamic Cosmological Simulations

Ying Zu^{1*}, David H. Weinberg^{1,2,3}, Romeel Davé⁴, Mark Fardal⁵, Neal Katz⁵, Dušan Kereš⁶, Benjamin D. Oppenheimer⁷

¹*Department of Astronomy, The Ohio State University, 140 W. 18th Avenue, Columbus, OH 43210, USA*

²*Center for Cosmology and Astro-Particle Physics, The Ohio State University, Columbus, OH 43210*

³*Institute for Advanced Study, Princeton, NJ 08540*

⁴*Astronomy Department, University of Arizona, Tucson, AZ 85721, USA*

⁵*Department of Physics and Astronomy, University of Massachusetts at Amherst, Amherst, MA 98105*

⁶*Institute for Theory and Computation, Harvard-Smithsonian Center for Astrophysics, Cambridge, MA 02138, USA*

⁷*Leiden Observatory, Leiden University, 2300 RA Leiden, The Netherlands*

23 October 2018

ABSTRACT

Recently Ménard et al. (hereafter MSFR) detected a subtle but systematic change in the mean color of quasars as a function of their projected separation from foreground galaxies, extending to comoving separations of $\sim 10h^{-1}\text{Mpc}$, which they interpret as a signature of reddening by intergalactic dust. We present theoretical models of this remarkable observation, using smoothed particle hydrodynamic (SPH) cosmological simulations of a $(50h^{-1}\text{Mpc})^3$ volume. Our primary model uses a simulation with galactic winds and assumes that dust traces the intergalactic metals. The predicted galaxy-dust correlation function is similar in form to the galaxy-mass correlation function, and reproducing the MSFR data requires a dust-to-metal mass ratio of 0.24, about half the value in the Galactic ISM. Roughly half of the reddening arises in dust that is more than $100h^{-1}\text{kpc}$ from the nearest massive galaxy. We also examine a simulation with no galactic winds, which predicts a much smaller fraction of intergalactic metals (3% vs. 35%) and therefore requires an unphysical dust-to-metal ratio of 2.18 to reproduce the MSFR data. In both models, the signal is dominated by sightlines with $E(g-i) = 0.001 - 0.1$. The no-wind simulation can be reconciled with the data if we also allow reddening to arise in galaxies up to several $\times 10^{10} M_{\odot}$. The wind model predicts a mean visual extinction of $\langle A_V \rangle \approx 0.0133$ mag out to $z = 0.5$, with a sightline-to-sightline dispersion similar to the mean, which could be significant for future supernova cosmology studies. Reproducing the MSFR results in these simulations requires that a large fraction of ISM dust survive its expulsion from galaxies and its residence in the intergalactic medium. Future observational studies that provide higher precision and measure the dependence on galaxy type and environment will allow detailed tests for models of enriched galactic outflows and the survival of intergalactic dust.

Key words: galaxies: formation — intergalactic medium

1 INTRODUCTION

Heavy element enrichment in intergalactic gas has long been studied via absorption lines in quasar spectra and, in more restricted regimes, via the influence of metal species on the X-ray emission spectra of clusters and groups. In the Galactic interstellar medium (ISM), roughly half of the mass of heavy elements is in solid phase — interstellar dust — which is thought to contain roughly 2/3 of interstellar carbon and the great majority of interstellar magnesium, silicon, and iron (Draine 2009 and references therein). This

solid-phase material is much more difficult to study in the intergalactic medium (IGM), in part because the expected level of dust extinction along any given line of sight is small, and in part because the continuum spectra of potential background sources — quasars, galaxies, and supernovae — show much greater variation than those of spectroscopically typed stars. In a recent breakthrough study, Ménard et al. (2009, hereafter MSFR) used large samples of quasars and galaxies from the Sloan Digital Sky Survey (SDSS; York et al. 2000) to measure reddening by intergalactic dust, detecting a systematic change in quasar colors with increasing distance from foreground galaxies, measured to comoving projected separations of $\sim 10h^{-1}\text{Mpc}$. In this paper, we use hy-

* E-mail: yingzu@astronomy.ohio-state.edu

hydrodynamic cosmological simulations to provide the first theoretical models of the MSFR results and to infer their implications for galactic outflows and the survival of dust in the IGM.

Ever since Chandrasekhar & Münch (1952) modeled the opacity of interstellar matter using angular correlation statistics in the brightness fluctuations of the Milky Way, there have been efforts to constrain the presence of a diffuse dust component outside the Galaxy by measuring the extinction of background objects. Zwicky (1962) first claimed the existence of intracluster dust in Coma based on the extinction of light from background clusters, though his inferred level is certainly incompatible with more modern constraints. Quasars are powerful “backlights” for studying the transparency of the Universe across a wide range of cosmic time. Ostriker & Heisler (1984) modeled the effects of uniform and clumped dust distributions on the redshift evolution of quasar luminosity functions, but they concluded that observations did not clearly favor one specific dust distribution over another. Taking advantage of the efficiency and accurate calibration afforded by CCD observations, Zaritsky (1994) averaged hundreds of background galaxies to detect a mean color excess of $E(B - I) \sim 0.067$ behind two nearby galactic halos, arguing for the existence of dust out to at least $60h^{-1}$ kpc. Ménard et al. (2008) also found evidence of dust in the halos of L_* galaxies via studies of MgII absorbers. Confirming both findings, Kaneda et al. (2009) presented a direct detection of extended far-IR dust emission in the halo of NGC 253. The existence of dust in the intracluster medium has remained controversial, however, as reviewed by Muller et al. (2008), who derived $E(B - R) = 0.005 \pm 0.008$ from galaxies behind 458 RCS clusters. Using a larger sample of $\sim 10^4$ clusters from the SDSS, Chelouche et al. (2007) obtained significant detections of $E(g - i) \approx \text{few} \times 10^{-3}$ out to several virial radii using the average colors of background quasars. Bovy et al. (2008) inferred upper limits at roughly the same level for a sample of $z \approx 0.05$ SDSS clusters using the spectra of early-type galaxies, though their results are not clearly inconsistent with Chelouche et al.’s.

MSFR instead examined the mean colors of 85,000 photometrically identified quasars (Richards et al. 2004) as a function of angular separation from 20 million foreground galaxies in a 3800 square degree sky area from the SDSS. They also used the quasar brightnesses to infer the galaxy-mass correlation function from weak lensing magnification. They found that the galaxy-dust and galaxy-mass correlation functions track each other remarkably well, with a correlated dust surface density profile $\Sigma_{\text{dust}} \propto \theta^{-0.8}$ detected out to angular separations that correspond to $\sim 10h^{-1}$ Mpc. The color dependence of the reddening signal is consistent with “standard” interstellar dust, though the constraints are loose, implying $R_V \equiv A_V/E(B - V) = 3.9 \pm 2.6$. The MSFR results provide direct evidence for extended intergalactic dust absorption, with an inferred total dust mass comparable to the amount of dust in galaxy disks.

Our primary model in this paper is based on a cosmological smoothed particle hydrodynamics (SPH) simulation that incorporates the momentum-driven galactic wind prescription of Oppenheimer & Davé (2006), which successfully matches several observed aspects of gas-phase metal enrichment in galaxies and the IGM (see references in §2). In momentum-driven wind models, radiation pressure on dust grains is the primary mechanism that sweeps gas out of galaxies (Murray et al. 2005). We do not attempt to model the survival of dust in the IGM; rather, we treat the ratio of dust mass to heavy element mass as a free parameter to be inferred by matching the MSFR reddening measurements. The metallicity of the outflowing gas is assumed to equal that of the star-forming

gas, whose associated star formation effectively powers the outflow with radiation pressure. The model here is almost the converse of the one treated by Aguirre et al. (2001), who considered radiative expulsion of dust (without gas entrainment) and subsequent destruction as a source of IGM gas enrichment. As alternatives to the momentum-driven wind scenario, we also consider two models based on an SPH simulation without galactic winds. The first assumes that the MSFR reddening signal arises in the simulation’s enriched intergalactic gas, which comes mainly from ram pressure and tidal stripping in groups and clusters. The second model allows additional absorption in low mass galaxies.

We hope to address a number of questions inspired by the MSFR observations. Can the simulation with galactic winds explain these observations? What dust-to-metal mass ratio is required to do so, and what does this imply about the survival of dust in the IGM? How is the dust distributed in the simulation? Do the models without galactic winds provide a viable alternative explanation of the MSFR findings? What further observations can test the model predictions and provide greater insight into the origin and evolution of intergalactic dust?

Section 2 describes our simulations and presents visual maps of the predicted spatial distribution of intergalactic metals. Section 3 presents our main results, including the predicted galaxy-dust correlations and projected reddening profiles, the contributions to the reddening signal from gas at different distances from high mass galaxies, the relative amounts of galactic and intergalactic dust, and the cumulative distribution functions of dust reddening. In section 4, we briefly discuss the issues of dust survival and extinction of high-redshift supernovae. Section 5 summarizes our results with a look to potential future directions for observational studies.

2 SIMULATIONS AND METAL DISTRIBUTIONS

The simulations are performed using our modified (Oppenheimer & Davé 2008) version of GADGET-2 (Springel 2005), which combines a tree-particle-mesh algorithm for gravitational calculations with smoothed particle hydrodynamics (SPH, Lucy 1977; Gingold & Monaghan 1977). The cosmological parameters are $\Omega_m = 0.25$, $\Omega_\Lambda = 0.75$, $\Omega_b = 0.044$, $H_0 = 70 \text{ km s}^{-1} \text{ Mpc}^{-1}$, $\sigma_8 = 0.8$ and $n = 0.95$, in good agreement with 5-year *Wilkinson Microwave Anisotropy Probe* (WMAP) results (Hinshaw et al. 2009). We simulated the evolution of 288^3 dark matter particles and the same number of gas particles in a periodic box with a comoving size $50h^{-1}$ Mpc on a side. The gas particle mass is $m_{\text{SPH}} = 9 \times 10^7 M_\odot$, and the gravitational spline force softening is $\epsilon = 4.9h^{-1}$ kpc (comoving; equivalent to Plummer softening $\epsilon = 3.5h^{-1}$ kpc). We identify galaxies using the program SKID¹, which selects groups of stars and cold ($T < 3 \times 10^4$ K), dense ($\rho/\bar{\rho}_{\text{baryon}} > 1000$) gas particles that are associated with a common density maximum. Convergence tests indicate that the simulations resolve galaxies with baryonic mass (stars plus cold gas) greater than $\sim 64m_{\text{SPH}}$, corresponding to $5.8 \times 10^9 M_\odot$.

One of our simulations is similar to the L50/288 run analyzed by Kereš et al. (2009a,b), with slightly different cosmology. Star formation happens in a sub-resolution two-phase medium, where thermal energy deposited by the supernovae pressurizes the gas but

¹ <http://www-hpcc.astro.washington.edu/tools/skid.html>

Table 1. Gas-phase Metal Mass in the Two Simulations

Model	All Z ($10^{10} M_{\odot}$)	free Z ($10^{10} M_{\odot}$)
Wind	288.0	100.7 (35.0%)
No-Wind	277.9	8.2 (3%)

does not drive outflows. We refer to the intergalactic dust distribution of this simulation as the “No-Wind Model.”

Our second simulation uses the same cosmological and numerical parameters as the first one, but it incorporates the kinetic feedback wind mechanism of GADGET-2 with the “momentum-driven wind” scalings of Oppenheimer & Davé (2006); we refer to the intergalactic dust distribution of this simulation as the “Wind Model.” Motivated by the analytical model of Murray et al. (2005), this second simulation scales the wind velocity with the velocity dispersion σ of the galactic halo and the mass loading factor (the ratio of gas ejection rate to star formation rate) with σ^{-1} . The implementation is discussed in more detail by Oppenheimer & Davé (2008), though the simulation in that paper has slightly different parameters. Simulations with this wind implementation successfully match observations of early IGM enrichment (Oppenheimer & Davé 2006), the galaxy mass-metallicity relation (Finlator & Davé 2008), OVI absorption at low redshift (Oppenheimer & Davé 2009), enrichment and entropy levels in galaxy groups (Davé et al. 2008), and the sub- L_* regime of the galaxy baryonic mass function (Oppenheimer et al. 2010). However, there are both physical and numerical uncertainties in this wind implementation, so we take it as a representative illustration of how galactic winds could influence intergalactic dust. For the purposes of our investigation, the key features of the wind model are the total amount of metals expelled and the typical scale over which they are distributed.

The median redshift of the MSFR galaxy sample is $\langle z \rangle \simeq 0.36$, and the effective luminosity² is $\sim 0.45 L_*$, with a corresponding comoving space density of $n_g \sim 0.01 h^3 \text{Mpc}^{-3}$ (Blanton et al. 2003). To reasonably approximate the MSFR sample, we analyze the $z = 0.3$ redshift outputs of the two simulations and apply a galaxy baryonic mass cut of $5.4 \times 10^{10} M_{\odot}$ ($\sim 600 m_{\text{SPH}}$), which yields $n_g = 0.01 h^3 \text{Mpc}^{-3}$ in the Wind Model. We apply the same galaxy baryonic mass cut to the No-Wind Model, though in this case the comoving space density is higher, $n_g = 0.033 h^3 \text{Mpc}^{-3}$. We enforce the same mass cut rather than the same number density for the two galaxy samples so that we are comparing two similar populations of galaxies (with typical luminosity $\sim 0.45 L_*$) in different simulations.³ Note that we quote comoving distances throughout the paper, and unless otherwise stated, the “galaxies” we refer to are those above the mass threshold. Since we are interested in modeling the reddening signal that is *correlated* with galaxies, we do not need to include extinction that might arise at lower or higher redshift than our simulation box, which would pro-

duce a mean shift and dispersion in quasar colors that is uncorrelated with the galaxy population in our simulation volume.

Four heavy elements (C, O, Si and Fe) are tracked in the simulation. In this exploratory work, we simply choose the total gas-phase metallicity as the tracer of cosmic dust, because the amount of dust should be proportional to the metal available if we assume the relative proportions of refractory elements depend weakly on enrichment. We define “free metals” to be those in gas particles that are not associated with *any* SKID group (i.e., with no mass cut applied); recall that the SKID density threshold is $\rho/\bar{\rho}_{\text{baryon}} > 1000$, low enough to include gas in extended regions of the interstellar medium. We generally include only these “free metals” when computing the intergalactic dust extinction for comparison to MSFR, on the assumption that quasars behind the optically thick disks of galaxies will not make it into the SDSS sample because of obscuration. The disks of bright galaxies cover a small fraction of the sky in any case. However, for the No-Wind simulation we also consider a “hybrid dust” calculation in which we include metals in galaxies below $5.4 \times 10^{10} M_{\odot}$, allowing the possibility of the MSFR signal arising in low luminosity galaxies.

Table 1 lists the total mass of all gas-phase metals (interstellar plus intergalactic) and all free metals (intergalactic only) in the two simulations. The total gas-phase metal mass is nearly identical in the two cases. This agreement is somewhat coincidental, as the No-Wind simulation forms more stars but leaves a larger fraction of its metals locked up in stars and stellar remnants. The mass of *free* metals in the Wind simulation is 12 times higher, as much of the enriched gas is ejected from galaxies. The top panels of Figure 1 show the projected density distribution of free metals from the two models in a $25 h^{-1} \text{Mpc} \times 25 h^{-1} \text{Mpc}$ slice of $5 h^{-1} \text{Mpc}$ thickness; the lower panels show a $5 h^{-1} \text{Mpc} \times 5 h^{-1} \text{Mpc}$ zoom on the densest region of the slice. In these densest regions the free metal distributions of the two models are fairly similar, tracing the galaxy distributions inside groups and clusters. Intergalactic metals in the No-Wind simulation presumably come from a combination of tidal and ram pressure stripping, an enrichment process first highlighted by Gnedin & Ostriker (1997). However, free metals in the No-Wind simulation arise *only* in these dense group and cluster environments, where stripping mechanisms can operate effectively. The Wind simulation shows much more widely distributed metals, in smaller halos and in the filaments that connect them. Thus, the two simulations differ dramatically in the total amount of free metals and in the spatial distribution of these metals.

Large (small) circles in the lower panels mark zones of radius $100 h^{-1} \text{kpc}$ ($30 h^{-1} \text{kpc}$) around SKID groups more (less) massive than $5.4 \times 10^{10} M_{\odot}$, which we will refer to in our analysis below. The spatial distributions of SKID groups are similar in the two simulations, though masses are systematically lower in Wind simulation, converting some large circles to small circles.

3 GALAXY-DUST CORRELATIONS AND QUASAR REDDENING

Figure 2 shows 3-dimensional auto- and cross-correlation functions from the two simulations. For the cross-correlation functions, we compute the (dark matter, gas, metal, or free metal) mass of neighboring particles in spherical shells of successive radii, ranging from $10 h^{-1} \text{kpc}$ to $5 h^{-1} \text{Mpc}$ with logarithmic intervals, average over all galaxies above our $5.4 \times 10^{10} M_{\odot}$ threshold, and normalize by the mass expected in a randomly located shell of equal volume. The two dark matter autocorrelation functions are nearly identical, as

² The effective luminosity is defined as the metallicity weighted mean luminosity of the galaxy sample, assuming the metallicity-luminosity relation of Tremonti et al. (2004) and a Schechter luminosity function with $\alpha = -1.1$.

³ If we instead select a sample with $n_g \sim 0.01 h^3 \text{Mpc}^{-3}$ in the No-Wind simulation, the galaxy-mass correlation rises by 1.4; our main conclusions about the No-Wind model are immune to rescaling the galaxy-dust correlation function by such a factor.

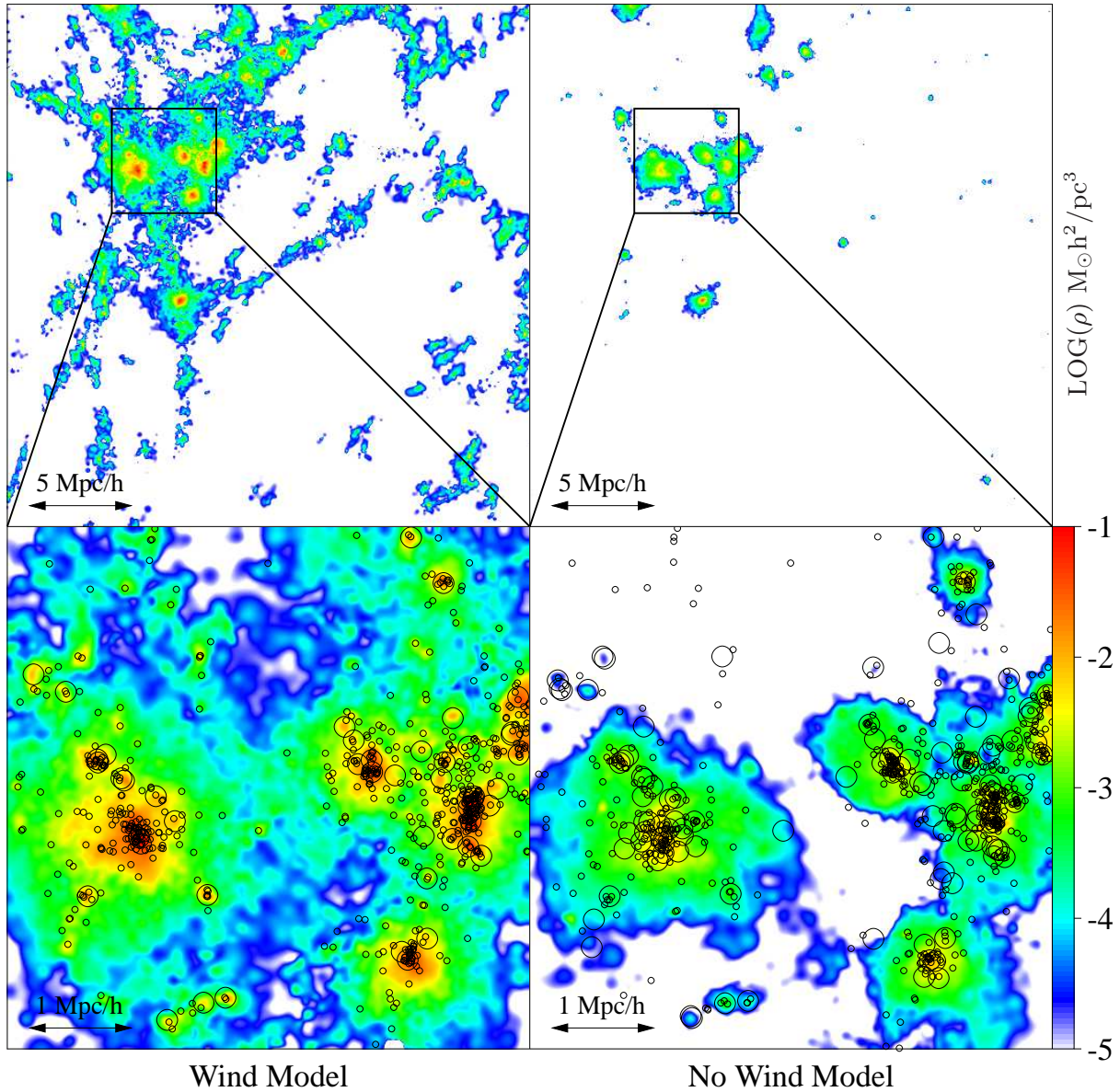


Figure 1. Surface density maps of the free metals (i.e., metals not in galaxies) in the Wind Model (Left) and the No-Wind Model (Right), at redshift $z = 0.3$. Top panels show a $25h^{-1}\text{Mpc} \times 25h^{-1}\text{Mpc} \times 5h^{-1}\text{Mpc}$ (comoving) slice for each model, with the density scale color coded as in the bottom-left color bar. Bottom panels show $(5h^{-1}\text{Mpc})^3$ cubes zoomed into the densest region of the top two panels. Large circles of $100h^{-1}\text{kpc}$ radius indicate the positions of SKID groups more massive than $5.4 \times 10^{10} M_{\odot}$, and small circles of $30h^{-1}\text{kpc}$ radius mark those less than $5.4 \times 10^{10} M_{\odot}$.

expected since the simulations have the same initial conditions and the gravitational impact of wind feedback is tiny. The galaxy autocorrelation and galaxy-dark matter cross-correlation are slightly higher in the Wind Model (compare to the dark matter autocorrelation at large scales) because in this simulation our $5.4 \times 10^{10} M_{\odot}$ mass threshold picks out rarer objects with a stronger clustering bias.

Turning to collisional components, the galaxy-gas correlation in the No-Wind Model tracks the dark matter autocorrelation on scales $> 1h^{-1}\text{Mpc}$, then falls below it at $r < 0.5h^{-1}\text{Mpc}$ until rising steeply inside $20h^{-1}\text{kpc}$ because of dissipational condensation into disks. The deficit at intermediate scales probably reflects the removal of gas from the inner regions of halos by this condensation, and its subsequent conversion to stars. The galaxy-gas correlation in the Wind Model tracks the dark matter autocorrelation until

the sharp upturn of the former inside $30h^{-1}\text{kpc}$. The absence of an intermediate-scale deficit could be an effect of gas redistribution by winds, or it could reflect the lower amount of stellar conversion in this simulation. The galaxy-metal correlations trace the galaxy-galaxy correlations beyond $0.5h^{-1}\text{Mpc}$ in both simulations, which is unsurprising since most of the metals reside in galaxies. However, in the No-Wind Model the cross-correlation of galaxies with *free* metals is much higher amplitude, by roughly a factor of two at all scales, because the free metals in this model arise only in group and cluster regions, which are highly biased relative to galaxies and dark matter.

To facilitate comparison with observations, we concentrate on the direct observable in the MSFR paper, the average reddening profile around galaxies, $\langle E(g-i) \rangle_g$, inferred from the change in quasar colors as a function of projected separation. Note that

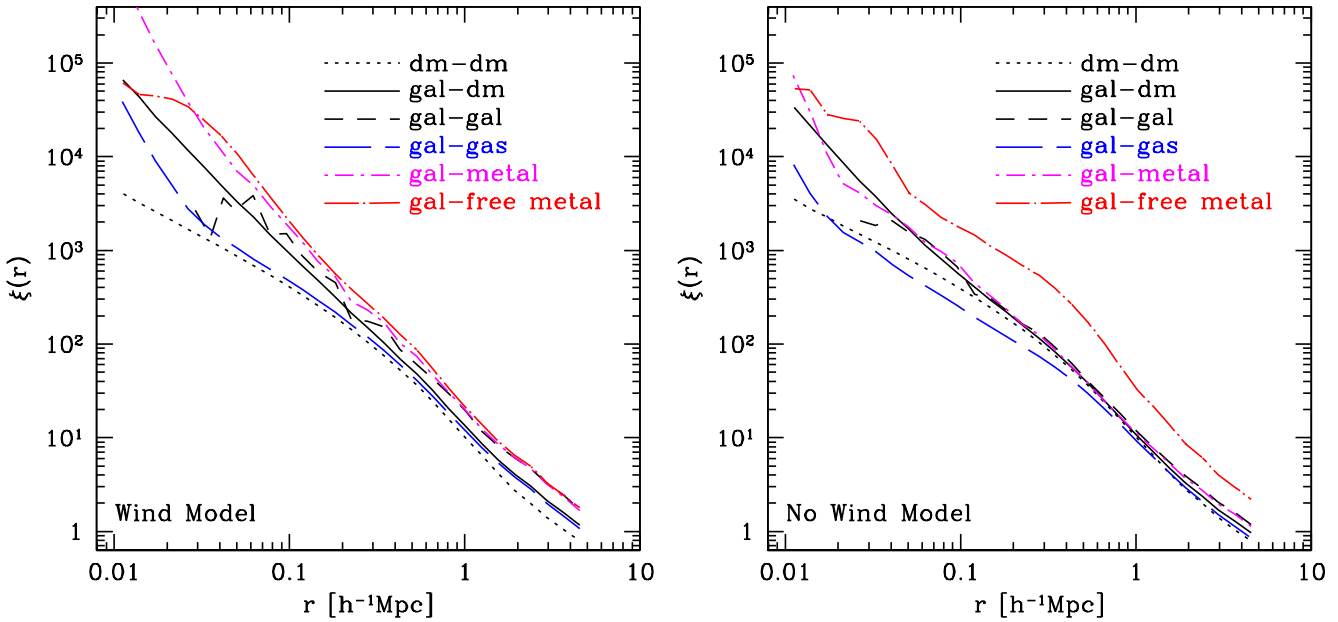


Figure 2. 3-dimensional correlation functions in the Wind Model (left) and No-Wind Model (right). Black dotted, solid, and dashed lines show the dark matter autocorrelation, galaxy-dark matter cross-correlation, and galaxy autocorrelation functions, respectively. Blue dashed lines show the galaxy-gas cross-correlation. Magenta and red dot-dashed lines show the cross-correlation of galaxies with all metals (short dashes) and free metals (long dashes), respectively.

we adopt comoving transverse distance r_p rather than the angular/physical distance in the MSFR paper. To estimate $\langle E(g-i) \rangle_g$, we first calculate the projected correlation function $w(r_p)$ between galaxies and free metals in the two models by directly summing metals through the simulation cube in annuli around galaxies, using x , y , and z projections. We then convert $w(r_p)$ to an average free-metal density profile, which we convert to an excess dust surface density profile $\Sigma_d(r)$ by multiplying by a dust-to-metal ratio $R_{d/m}$. We convert $\Sigma_d(r)$ to a rest-frame reddening profile $\langle E(g-i) \rangle_g$ assuming SMC-type dust as justified in MSFR, specifically

$$\langle E(g-i) \rangle_g \simeq 1.52 \langle E(B-V) \rangle_g = \frac{3.8}{\ln(10)} \frac{K_{\text{ext}}(\lambda_V)}{R_V} \Sigma_d(r), \quad (1)$$

where the factor 1.52 comes from the conversion between two colors adopting an extinction law $A_\lambda \propto \lambda^{-1.2}$ and $K_{\text{ext}}(\lambda_V) \simeq 1.54 \times 10^4 \text{ cm}^2 \text{ g}^{-1}$ is the absorption cross section per mass of SMC dust in V-band. We choose the value of $R_{d/m}$ to match the MSFR data point at $r_p = 1 h^{-1} \text{ Mpc}$. While our standard calculation simply assigns all the metals associated with a particle to the annulus in which it resides, we have checked that smoothing the metals over the SPH kernel before projecting yields indistinguishable reddening profiles.

Figure 3 shows the central result of this paper, predicted reddening profiles (solid black curves) for the Wind Model (left) and No-Wind Model (right), in comparison to the MSFR data points (from their Figure 6). By construction, the model curves go through the MSFR data point at $r_p = 1 h^{-1} \text{ Mpc}$. For the Wind Model, this normalization requires $R_{d/m} = 0.24$, i.e., 24% of the free metal mass is in the form of dust. In the Milky Way interstellar medium, roughly 50% of the metal mass is in dust (Draine 2009), so $R_{d/m} = 0.24$ is physically plausible, but it requires that a large fraction of the dust formed in the ISM survive the journey to and sojourn in intergalactic space. Given the normalization

at $1 h^{-1} \text{ Mpc}$, the model reproduces the shape of the MSFR profile fairly well from $r_p = 20 h^{-1} \text{ kpc}$ out to $r_p = 5 h^{-1} \text{ Mpc}$, beyond which box-size effects can artificially depress the model predictions. MSFR show empirically that the galaxy-dust correlation function approximately follows the galaxy-mass correlation function, which is what we find theoretically for the galaxy-free metal correlation function (Figure 2), so the approximate agreement of shape is unsurprising.

For the No-Wind Model, the free metals would be insufficient to explain MSFR reddening even if all of them were depleted onto dust (gray solid line on the right panel). Matching the MSFR normalization requires $R_{d/m} = 2.18$, i.e., 218% of the metal mass in dust (black solid line on the right panel). This is physically impossible, of course, but a change in the dust grain size distribution from the SMC dust assumed here could possibly achieve more efficient reddening for a given amount of metal mass. In detail, neither model perfectly reproduces the shape of the MSFR data at $r_p < 1 h^{-1} \text{ Mpc}$, where the “1-halo” regime of clustering begins to dominate over the “2-halo” regime (see, e.g., Peacock & Smith 2000; Berlind & Weinberg 2002). The agreement is worse for the No-Wind Model, where the halos hosting most of the intergalactic dust are typically larger (see Figure 1). However, when we analyze the three box projections individually, we find $\sim 30\%$ variations from one to another, so we do not attribute much weight to these discrepancies at present; we are also comparing predictions at fixed redshift to inferences from angular correlations over a range of redshift. Blue curves in Figure 3 show the predicted reddening profiles in the two models if we assume that dust traces intergalactic gas rather than intergalactic metals. The MSFR normalization can be reproduced for dust-to-gas mass ratios of 2.3×10^{-4} (Wind Model) or 3.1×10^{-4} (No-Wind Model), comparable to those inferred from observations of dwarf galaxies (Lisenfeld & Ferrara 1998) and nearby galaxies (Issa et al. 1990). However, the dust-traces-gas reddening profiles flatten inside $r_p \approx 0.1 h^{-1} \text{ kpc}$, in contrast to

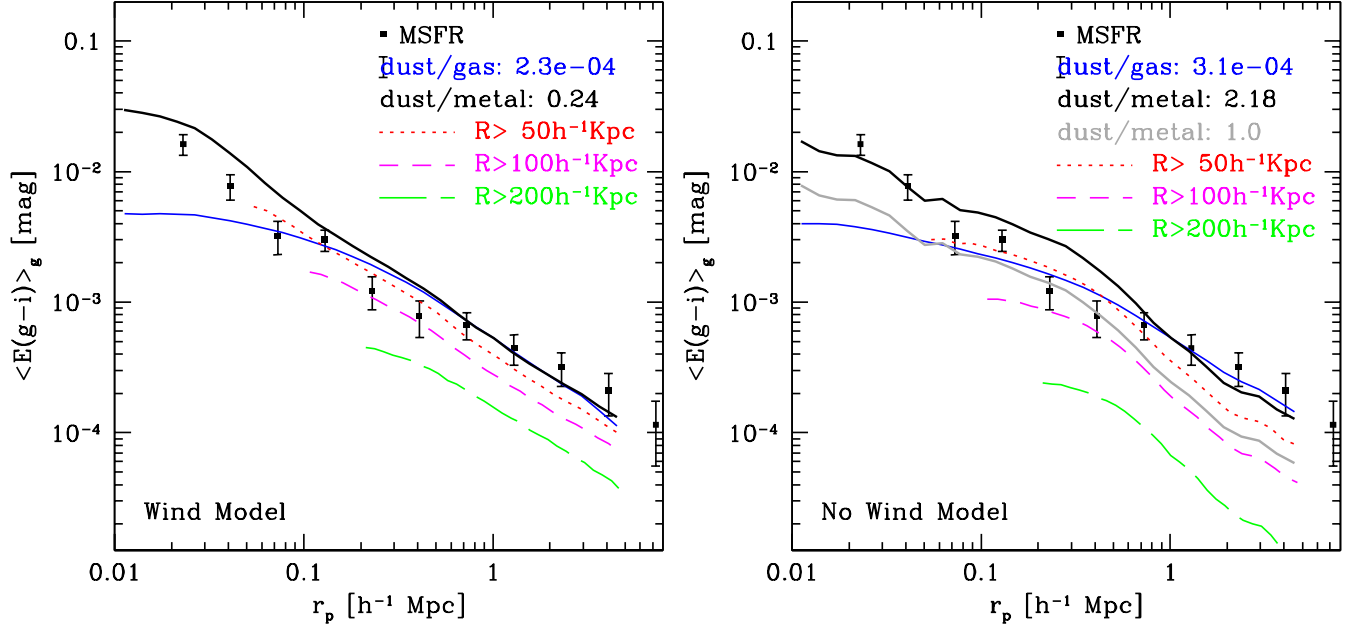


Figure 3. Average quasar reddening $\langle E(g-i) \rangle_g$ as a function of comoving transverse distance r_p to a foreground galaxy in the Wind Model (Left) and the No-Wind Model (Right). In each panel, solid squares with error bars are the observational results from MSFR. The blue (black) solid line is the predicted reddening profile assuming that dust traces gas (free metals), both normalized by matching the MSFR data point at $1h^{-1}\text{Mpc}$, with the dust-to-gas or dust-to-metal ratio indicated in the legend. Red dotted, magenta dashed and green long-dashed lines show the contribution to the reddening profile by metals respectively $50h^{-1}\text{kpc}$, $100h^{-1}\text{kpc}$, and $200h^{-1}\text{kpc}$ away from galaxies with baryonic mass $M > 5.4 \times 10^{10} M_\odot$. Reproducing the MSFR normalization in the No-Wind Model with SMC dust requires an unphysical dust-to-metal ratio of 2.18. The gray solid line in the right panel is the reddening profile for the No-Wind Model with SMC dust and a dust-to-metal ratio of unity.

the dust-traces-metal profiles and the MSFR data points. In principle, observations like those of MSFR can test hypotheses about the enrichment profiles of gas in galactic halos and the survival of dust as a function of distance from the source galaxy.

Dotted, short-dashed, and long-dashed lines in Figure 3 show the reddening profiles measured from the simulations if we eliminate sightlines that pass within 50, 100, or $200h^{-1}\text{kpc}$, respectively, of a galaxy above our $5.4 \times 10^{10} M_\odot$ threshold, keeping the dust-to-metal ratio the same. (Circles in Figure 1 show the $100h^{-1}\text{kpc}$ exclusion zones for comparison.) In the Wind Model, dust outside these three exclusion zones contributes 75%, 50%, and 30% of the overall reddening signal at large scales. In the No-Wind Model, the intergalactic dust is more tightly clumped around the massive galaxies, and the reddening signal drops more rapidly with radial exclusion, to 68%, 34%, and 12%, respectively. In addition to characterizing the radial scale of intergalactic dust in our simulations, these curves provide testable predictions of our models, which can be implemented observationally by eliminating quasars with small projected separations from foreground galaxies before computing the mean reddening profile.

Given the distinctive spatial patterns of the dust distributions in Figure 1, we expect the cumulative distribution functions (CDFs) of reddening to be quite different in the two models, with more of the total extinction in the Wind Model arising at very low $E(g-i)$ and more sightlines in the No-Wind Model being truly dust free. Figure 4 confirms this expectation. We calculate each reddening CDF by randomly picking sightlines within a given radial range around any galaxy (not necessarily the closest galaxy) on a pro-

jected reddening map generated by the *vista*⁴ command in TIPSYS⁵. The black histogram in each panel shows the reddening CDF in the projected separation bin at $50h^{-1}\text{kpc} < R < 100h^{-1}\text{kpc}$, while the green and red histograms show $200h^{-1}\text{kpc} < R < 300h^{-1}\text{kpc}$ and $1.0h^{-1}\text{Mpc} < R < 1.5h^{-1}\text{Mpc}$, respectively. The star on each histogram indicates the mean $E(g-i)$ value in the corresponding radial bin, and the black dashed line shows the mean amount of reddening in each simulation box. These mean extinction values are proportional to the total amount of dust in the simulation box, and thus to the comoving box length of simulation. In the Wind Model, the median reddening is $\approx 10^{-3}$ mag in the innermost radial bin, dropping to 10^{-4} mag and $10^{-4.4}$ mag in the next two bins. In the No-Wind Model, on the other hand, most sightlines are nearly dust free, with median reddening below 10^{-5} mag in all three radial bins. Only 3% of sightlines in the innermost bin for the Wind Model have reddening greater than 0.01 mag, and only 3.5% in the No-Wind Model. Unfortunately, because nearly all sightlines have a reddening level that is small compared to the intrinsic dispersion of quasar colors, the large differences in the CDFs of the two models are likely to be unobservable in practice.

The inset panels in Figure 4 show histograms of $E \cdot p(\log E)/\bar{E}$, the fractional contribution to the average $E(g-i)$ from each bin shown in the CDF. In the Wind Model, contributions to the mean reddening are broadly peaked in the range $E(g-i) = 0.001 - 0.03$ mag, shifting towards lower values for the

⁴ *vista* creates a fits image whose pixel values are smoothed quantities calculated by projecting the particles onto the grid using the SPH spline softening kernel.

⁵ <http://hpc astro.washington.edu/tools/tipsy/tipsy.html>

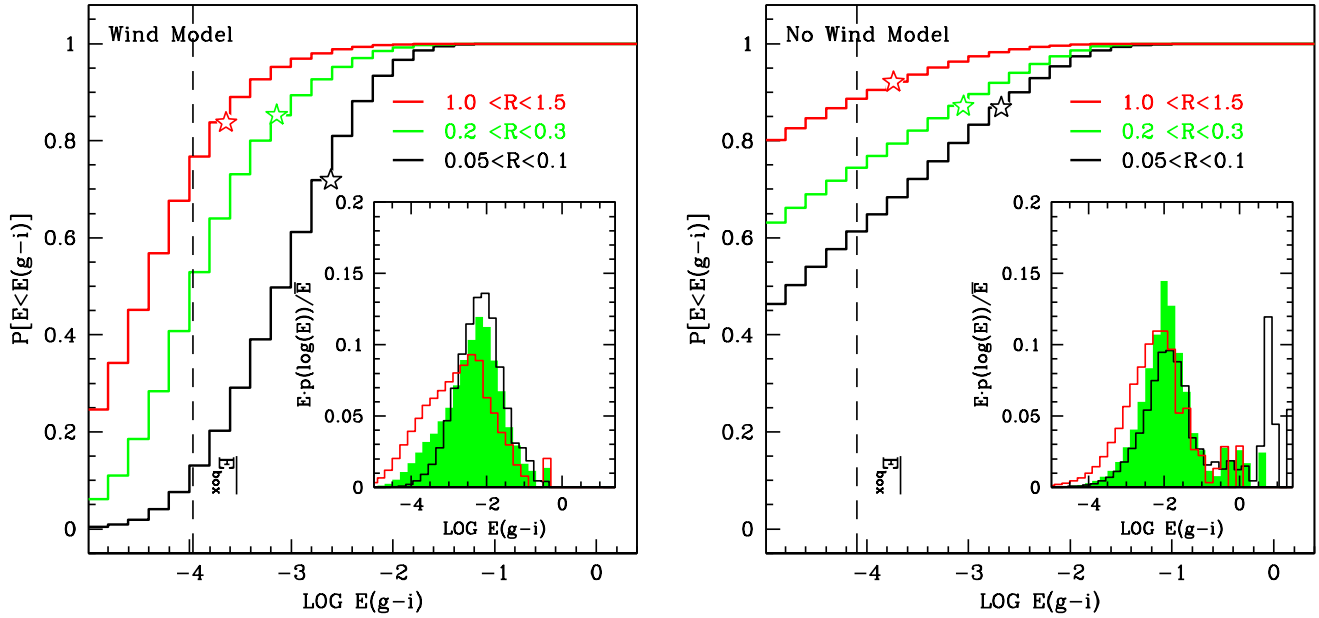


Figure 4. Cumulative distribution functions (CDFs) of reddening for three radial bins in the Wind Model (Left) and No-Wind Model (Right). In each panel, the black histogram shows the reddening CDF of quasars with projected separation $0.05h^{-1}\text{Mpc} < R < 0.1h^{-1}\text{Mpc}$ from a foreground galaxy, while green and red histograms show corresponding CDFs for separations $0.2h^{-1}\text{Mpc} < R < 0.3h^{-1}\text{Mpc}$ and $1.0h^{-1}\text{Mpc} < R < 1.5h^{-1}\text{Mpc}$, respectively. The black dashed line indicates the average amount of reddening through each simulation box, and the star on top of each histogram indicates the mean reddening value for the radial bin. Inset panels show histograms of $E \cdot p(\log(E))/E$, the fractional contribution from each $\log E(g-i)$ bin to the average amount of reddening marked by stars in the CDF. The histogram of each radial bin is indicated by the same color as in the main panel.

largest ($1 - 1.5h^{-1}\text{Mpc}$) radial separation bin. Contributions for the No-Wind Model also peak at 0.01 mag, though they continue up to strongly reddened sightlines with $E(g-i) = 0.1 - 0.6$ mag. However, even if these noticeably reddened quasars were eliminated from the sample (deliberately or by selection bias), the mean reddening profile would barely change.

Figure 5 compares the correlated reddening signal from intergalactic dust (tracing free metals) to the signal that would be contributed by including dust from galaxies below a succession of baryonic mass thresholds. We assume the same dust-to-metal mass ratio inside and outside of galaxies. Beyond $r_p \approx 30h^{-1}\text{kpc}$, the shapes of the correlated reddening profiles are all similar, tracking the shapes of the galaxy-galaxy and galaxy-mass correlation functions. When we consider dust in all galaxies (cyan dot-dashed line), the normalization for the No-Wind Model is ten times higher than that of the Wind Model, but this difference just reflects the higher dust-to-metal ratio assumed to match the free-metal prediction to the MSFR data. If we eliminate galaxies with baryonic mass $M > 5.4 \times 10^{10} M_\odot$, the reddening signal drops by a factor of six in the Wind Model but only a factor of three in the No-Wind Model. This difference reflects the greater efficiency of winds in ejecting metal-enriched gas from lower mass galaxies. If we consider only galaxies below $5.4 \times 10^{10} M_\odot$, the galactic dust is considerably less than the intergalactic dust in the Wind Model, but considerably more in the No-Wind Model. While the No-Wind Model has several times more mass in galaxies, and a higher space density of galaxies above a given mass threshold, the amount of metal mass (and hence dust) in the two simulations is similar (Table 1). The model differences in Figure 5 arise from the different distributions of metals inside and outside galaxies.

With intergalactic dust alone, the No-Wind Model requires

an unphysical ratio 2.18 of dust mass to metal mass to reproduce the MSFR data. However, Figure 5 shows that low mass galaxies contain much more metal mass than the intergalactic medium in the No-Wind Model. We therefore construct an alternative “hybrid dust” model from the No-Wind simulation, in which we include both dust associated with free metals and dust associated with low mass galaxies. The upper limit for the baryonic mass of those galaxies is $\sim \text{few} \times 10^{10} M_\odot$, largely determined by the total amount of metal (both free and inside faint galaxies) that is required to achieve a reasonable dust-to-metal ratio. For instance, if we include dust associated with galaxies with $M < 1.5 \times 10^{10} M_\odot$, the “hybrid dust” model would require 87% of the metals in the form of dust. The required dust-to-metal ratio drops to 60% if we increase the upper limit of low mass galaxies to $2.7 \times 10^{10} M_\odot$. To obtain a more reasonable dust-to-metal ratio ($0.1 < R_{d/m} < 0.5$), we need an upper limit of $\sim 5 \times 10^{10} M_\odot$. For the sake of uniformity of mass thresholds in the paper, we set $M = 5.4 \times 10^{10} M_\odot$ again to be the maximum baryonic mass of “faint” galaxies. Figure 6 shows the reddening profile and reddening CDF for this hybrid model, and Figure 7 compares the extinction map of this model to those of the Wind and No-Wind models. Reproducing the normalization of the MSFR measurements requires a physically acceptable dust-to-metal mass ratio of 0.39. The effect of excluding zones around high mass galaxies is similar to that in the Wind Model (compare the broken lines in the left panels of Figure 6 and Figure 3), except for a precipitous drop in the $R > 200h^{-1}\text{kpc}$ curve beyond $r_p = 3h^{-1}\text{Mpc}$. The reddening CDF is similar to that of the No-Wind Model (compare the right hand panels of Figures 4 and 6). While the addition of low mass galaxies reduces the number of truly metal-free sightlines, the factor of 5.5 reduction in the dust-to-metal mass ratio compensates by shifting the previously obscured

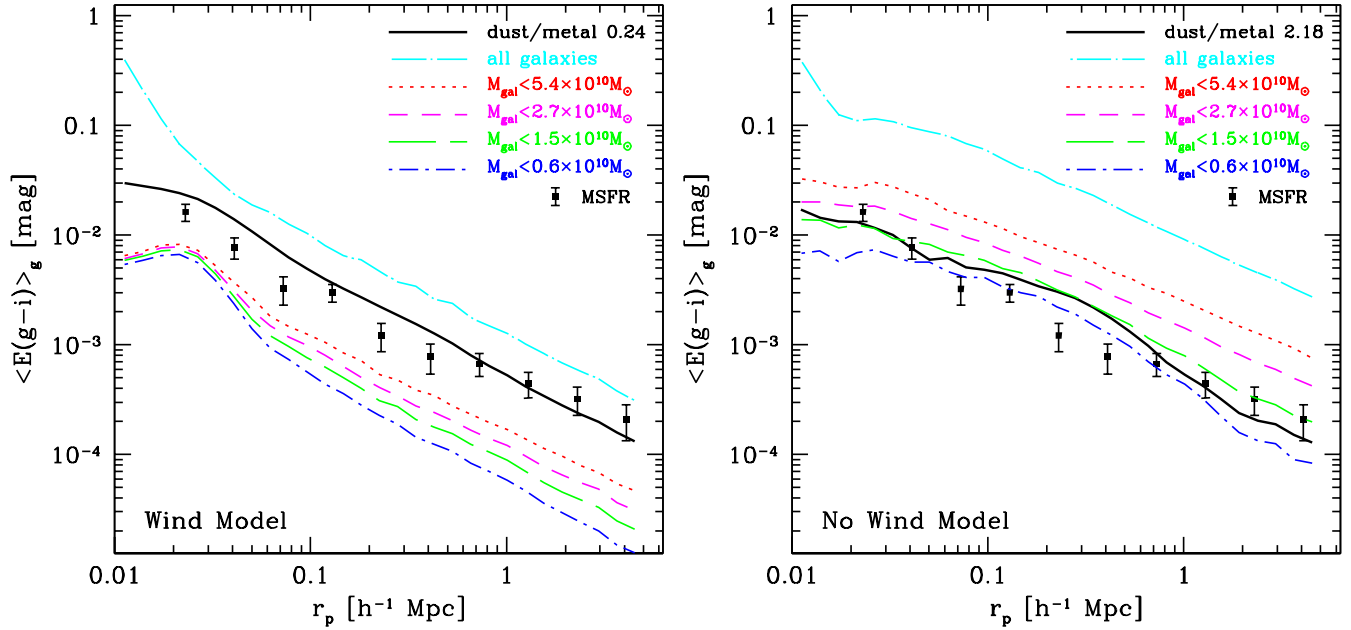


Figure 5. Reddening caused by dust in low mass galaxies in the Wind Model (Left) and No-Wind Model (Right). In each panel, solid squares are from MSFR, and solid black lines show the reddening produced by intergalactic gas assuming a constant dust-to-metal ratio on all scales as in Fig. 3. Blue dot-dashed, green long-dashed, magenta dashed, and red dotted, lines indicate the additional reddening when including dust contained by galaxies with masses less than 0.6 , 1.5 , 2.7 , and $5.4 \times 10^{10} M_{\odot}$, respectively. The sum of one of these curves with the black curve shows the reddening predicted if the MSFR sample included quasars behind galaxies lower than the corresponding mass threshold, assuming the same dust-to-metal mass ratio both inside and outside of galaxies. Cyan dot-dashed lines (the highest in each panel) show the reddening from dust in *all* galaxies.

sightlines to lower reddening values. One can see this behavior in the extinction map of Figure 7: the extended blobs of free metals in groups and clusters shrink because of the lower dust normalization (the outer contours lie at a fixed reddening threshold of 10^{-4}), and they are supplemented by a peppering of dots that show the low mass galaxies tracing filamentary superclusters.

From the inset panel of Figure 6, one can see that the reddening distribution of the hybrid model is bimodal, with a “galactic” peak at high reddening and an “intergalactic” peak at low reddening. While sightlines with $E(g-i) > 0.1$ are rare, they contribute a large fraction of the mean reddening. These high reddening values might change quasar colors or magnitudes enough to throw them out of the quasar catalog used by MSFR for their measurement. Moreover, the light of the foreground galaxy itself might eliminate the background quasar from the input catalog, either by changing its color or by adding a detectable extended component that changes the object classification. At $z = 0.3$, a galaxy with baryonic mass $5.4 \times 10^{10} M_{\odot}$ has apparent magnitude $g \approx 20.4$, assuming a stellar mass-to-light ratio $M/L_g = 3M_{\odot}/L_{\odot}$, while the limit of the quasar catalog used by MSFR is $g \approx 21$. Thus, at least the brighter galaxies in the hybrid model would likely have a significant impact. We will not address the detailed selection questions here, but the clearest test of the hybrid model would be to search for signatures of blended galaxy light (perhaps by stacking the images of the selected quasars), as a function of separation from the bright foreground galaxies used for the cross-correlation measurement.

MSFR argue that the dust in LMC-like dwarfs is insufficient to explain the magnitude of their reddening signal. We concur with this conclusion. Reproducing the MSFR data in the hybrid model with a physical dust-to-metal mass ratio requires including galaxies up to several times $10^{10} M_{\odot}$, far larger than the $\sim 3 \times 10^9 M_{\odot}$ bary-

onic mass of the LMC (van der Marel et al. 2002). Furthermore, the No-Wind simulation predicts a galaxy baryonic mass function that is inconsistent with observations, with an excessive global fraction of baryons converted to stars (Oppenheimer et al. 2010)⁶. We do not consider the hybrid dust model to be nearly as plausible an explanation of the MSFR results as the Wind Model; we present it as a foil to illustrate what would be required to explain MSFR’s findings with dust in low mass galaxies. For the Wind Model, the metals in low mass galaxies contribute much less reddening than the intergalactic metals (Figure 5).

4 DISCUSSION

For the Wind Model to succeed, we require that the dust-to-metal mass ratio in the IGM be comparable to that in the ISM, allowing only $\sim 50\%$ of the ISM dust to be destroyed during its expulsion from galaxies and subsequent residence in the IGM. The validity of this assumption is by no means obvious, as the destruction timescales for $0.01 \mu\text{m}$ dust grains by thermal sputtering are $\sim 10^{7.5} (n_H/10^{-3} \text{ cm}^{-3})^{-1}$ years at $T = 10^6 \text{ K}$ (Draine & Salpeter 1979, Figure 7), while wind particles in the simulation typically remain in the IGM for $\sim 10^9$ years before reaccreting onto galaxies (Oppenheimer et al. 2010, Figure 2). However, the sputtering rates decline rapidly towards lower temperatures (e.g., a factor of 300 lower at $T = 10^5 \text{ K}$), and with the wind implementation used in this simulation most ejected gas never rises above a few $\times 10^4 \text{ K}$.

⁶ The Wind simulation predictions are reasonably consistent with the observed mass function for galaxies with $L < L_*$, though it still predicts excessive galaxy masses above L_* .

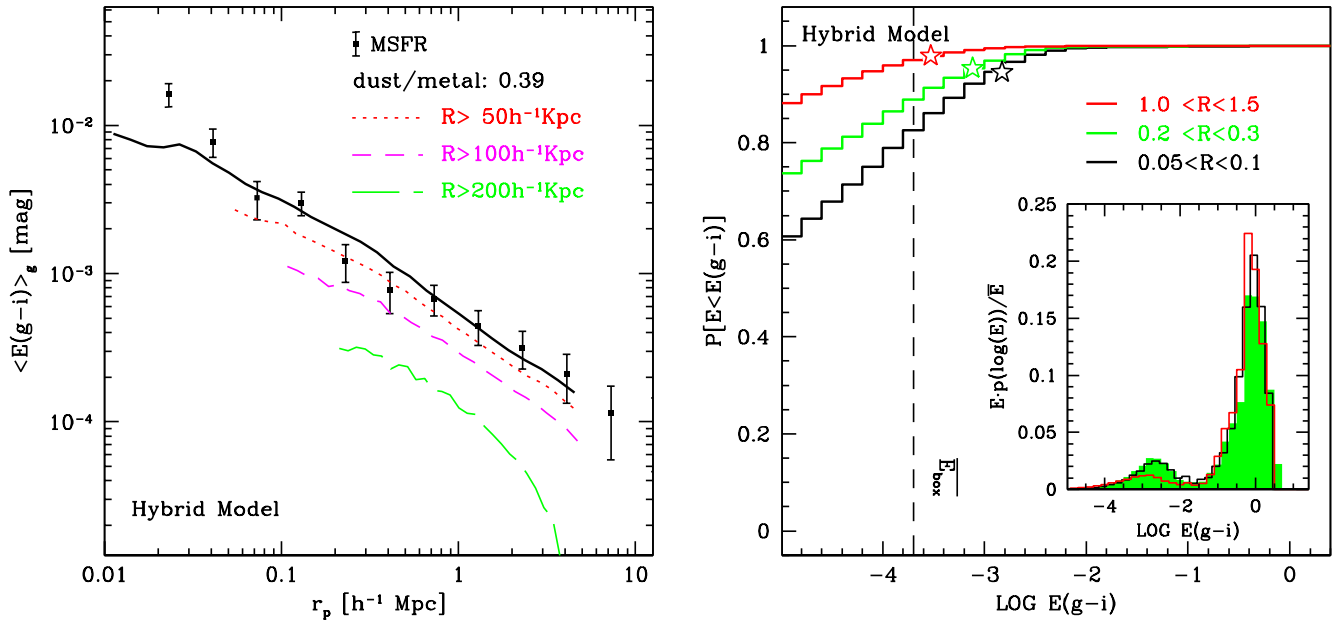


Figure 6. An alternative “hybrid” dust model including dust within low mass galaxies ($M < 5.4 \times 10^{10} M_{\odot}$) in the No-Wind simulation. *Left panel:* Comparison between extinction from hybrid dust (black solid line) and MSFR results (solid points). Red dotted, magenta dashed and green long-dashed lines indicate the extinction contribution from dust $50h^{-1}$ kpc, $100h^{-1}$ kpc and $200h^{-1}$ kpc away from high mass ($M > 5.4 \times 10^{10} M_{\odot}$) galaxies, respectively. *Right panel:* Cumulative distribution functions of reddening for the hybrid dust model. Black, green and red histograms show reddening CDFs of quasars in three bins of radial separation (from high mass galaxies), respectively $0.05 - 0.1$, $0.1 - 0.2$, and $1.0 - 1.5h^{-1}$ Mpc. The vertical dashed line indicates the average amount of reddening through the box, while the stars mark the mean extinction value for each radial bin. Inset panel shows the $E \cdot p(\log E) / \bar{E}$ for each radial bin, with the same format as Figure 4, but larger y -axis range.

UV or X-ray background photons are another possible destruction mechanism for IGM dust, but the intergalactic radiation field is much lower intensity than the radiation field dust grains already encounter in galactic star-forming regions.

A detailed consideration of dust survival in the IGM is beyond the scope of this initial investigation, but the MSFR results clearly raise it as an important subject for further study. The combination of their measurements with our models gives a fairly clear idea of what is required: survival of a substantial fraction of ejected dust, and an extinction curve that has roughly the color dependence of ISM dust. The temperature sensitivity of thermal sputtering could lead to preferential destruction of ejected dust in the higher mass halos that host a shock heated gas halo (see Birnboim & Dekel 2003; Kereš et al. 2005; Dekel & Birnboim 2006; Kereš et al. 2009). In the Wind Model, most wind particles in halos with $M < 10^{13} M_{\odot}$ have $T < 10^5$ K, but about 2/3 of the wind particles in halos with $M > 10^{13} M_{\odot}$ have $T > 3 \times 10^6$ K. If sputtering does destroy intergalactic dust at these temperatures, it could produce distinctive drops in the galaxy-reddening correlation when it is evaluated for massive galaxies or for galaxies in dense environments. The recent study of McGee & Balogh (2010), which examines the correlation of background quasar colors with projected separation from galaxy groups of varying richness, provides some hint of such an effect, but their innermost point is at $r = 1h^{-1}$ Mpc, close to the virial radius of typical group mass halos. Moreover, the Chelouche et al. (2007) measurements provide direct evidence for dust survival in the cluster IGM. Draine (2009) argues that ISM dust must form largely *in situ*, from the depletion of gas phase metals onto seed grains from supernovae and ejected stellar envelopes, and that the dust abundance is determined by an

equilibrium between growth and destruction mechanisms. Growth rates would be much slower in the low density IGM, but 2-body destruction processes would have the same density scaling, so a similar equilibrium abundance could arise.

Intergalactic dust could have an important impact on supernova cosmology studies, dimming and reddening supernovae increasingly with redshift. Given perfect knowledge of supernova intrinsic colors and the shape of the extinction curve, intergalactic extinction would be corrected automatically along with extinction in the supernova host galaxy. However, the intergalactic and host galaxy dust components could have different extinction curves, complicating the analyses. Furthermore, the presence of intergalactic dust means that no high-redshift supernovae have zero extinction, contrary to the assumption usually made in global models of the supernova population. MSFR give a rough estimate of the average extinction implied by their results, $\langle A_V \rangle = 0.03$ mag at $z = 0.5$, but the inference of a mean extinction from the *correlated* reddening signal is (as MSFR emphasize) sensitive to uncertain choices of radial profile cutoffs and luminosity extrapolations. (See Ménard et al. 2010 for further discussion.)

Our simulation provides an explicit physical model of the IGM metal distribution, and once the dust-to-metal mass ratio is set by matching the MSFR data, it is straightforward to compute the mean extinction by intergalactic dust. In the Wind Model, the comoving dust density $\rho_{\text{dust}} = 6.424 \times 10^{-35} \text{ g cm}^{-3}$. Assuming constant comoving dust density and extinction law $A_{\lambda} \propto \lambda^{-1.2}$, we can compute mean extinction to any given redshift z as

$$\langle A_V \rangle = \frac{2.5 K_{\text{ext}} c}{\ln(10)} \int_0^z (1+z)^{3.2} H(z)^{-1} \rho_{\text{dust}} dz, \quad (2)$$

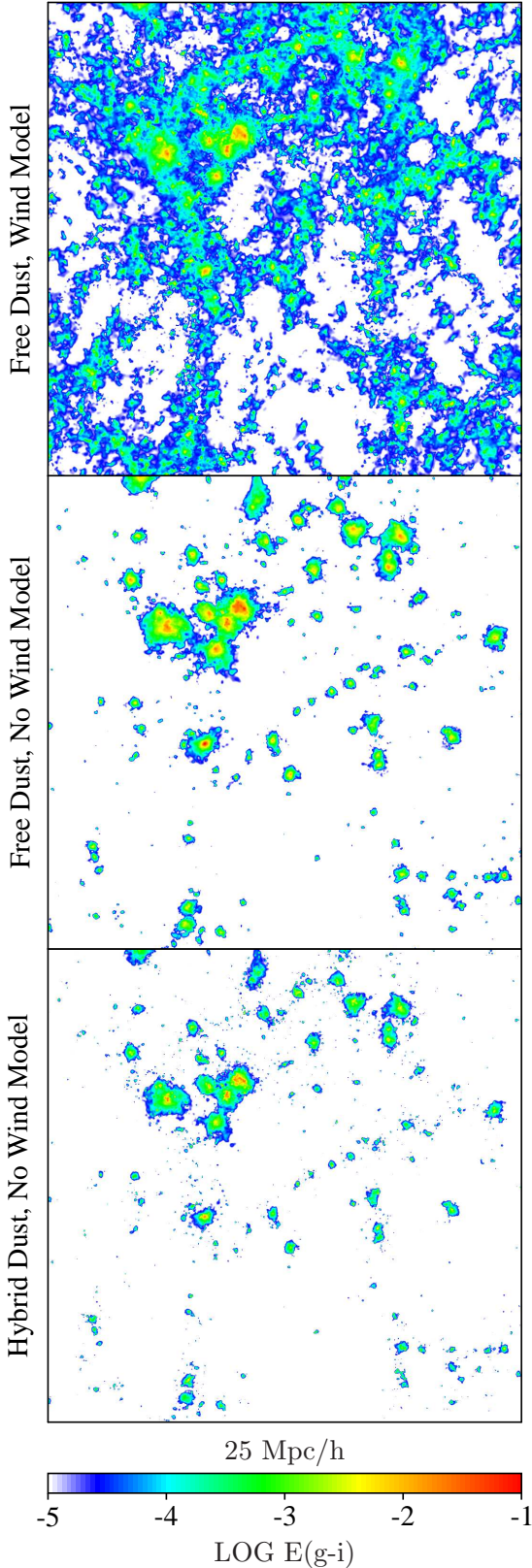


Figure 7. Comparison of reddening maps in the three dust models, each normalized to the MSFR result at $1h^{-1}\text{Mpc}$. The regions shown are a quadrant of the simulation cube, $25h^{-1}\text{Mpc} \times 25h^{-1}\text{Mpc} \times 50h^{-1}\text{Mpc}$. Red/blue regions indicate heavily/lightly reddened fields through the simulation, with the color scale running from $E(g-i) = 10^{-5}$ up to 0.1, logarithmically.

where $H(z)$ is the Hubble constant at redshift z , respectively. The $(1+z)^{3.2}$ term arises from the combination of cosmic areal expansion and rest-frame to observed V-band extinction conversion. This yields a predicted mean extinction $\langle A_V \rangle = 0.0133$ mag and a sightline-to-sightline variance of $\Delta^2 = (0.0272 \text{ mag})^2$ for supernovae at $z = 0.5$. More accurate estimates and an extrapolation to higher redshifts will require the combined analysis of many simulation outputs to track evolution. Our estimated extinction is small compared to the statistical and systematic errors of current surveys, but it is comparable to the ambitious goals set for next-generation surveys of several thousand high-redshift supernovae. At higher redshifts, furthermore, the (stronger) near-UV dust extinction gets redshifted into the observed-frame optical bands. We have assumed SMC dust for this calculation; since we normalize to MSFR's $E(g-i)$ measurements, the important assumption is the value of $A_V/E(g-i) = 4.7$.

5 SUMMARY

Compared to the element-by-element and sightline-by-sightline measurements of gas phase metals in quasar spectra, the correlation of galaxy separation and quasar color used by MSFR is a relatively blunt tool, requiring tens of thousands of background sources to yield a statistical detection of an intrinsically weak effect, and providing only a radial dependence and absolute normalization in several color bands. Nonetheless, this tool provides unique insight into an aspect of IGM enrichment that is virtually impossible to study by other means. We have investigated the ability of SPH cosmological simulations with and without galactic winds to explain MSFR's remarkable results.

The Wind Model, based on an implementation of galactic winds that has proven empirically successful in other contexts and is motivated by theoretical models of momentum-driven outflows, proves quite successful at reproducing the MSFR measurements, provided that about 25% of the metal mass in the IGM is in the form of SMC-like dust. This dust-to-metal mass ratio is roughly half that in the Milky Way ISM, so this normalization is reasonable provided dust survives its ejection from galaxies and its sojourn in the IGM. Accounting for dust depletion would lower the predicted level of intergalactic gas absorption in quasar spectra by $\sim 25\%$, at least for refractory elements such as carbon and silicon. In our Wind simulation, about 1/3 of the metals are intergalactic, and 2/3 are in galaxies (not counting the metals locked up in stars), with 60% of the latter in galaxies of baryonic mass $M > 5.4 \times 10^{10} M_\odot$. If we exclude sightlines that pass within 50, 100, and $200h^{-1}\text{kpc}$ of galaxies above this mass threshold, then the large scale correlated reddening signal drops to 75%, 50%, and 30% of the original signal, demonstrating the large scale of the distributed metals and providing an observationally testable diagnostic of the model (Figure 3). The cumulative distribution function (CDF) of reddening in each radial separation bin is a prediction that is testable in principle, but not in practice because the overall extinction is always dominated by sightlines with $E(g-i) < 0.03$ mag, small compared to the intrinsic dispersion of quasar colors.

The No-Wind simulation has just 3% of its metals in the intergalactic medium, almost all of it in the dense halos of groups and clusters where tidal interactions and ram pressure can strip enriched gas from member galaxies. The 3-dimensional cross-correlation function of galaxies with free metals is highly biased, but because the free metal fraction is so low to begin with, reproducing the MSFR data requires an unphysical dust-to-metal mass ratio of 2.18

in the IGM. This model could conceivably be made consistent with the data if the grain size distribution were altered to give more reddening for a given dust mass, though the consistency of the MSFR band-dependent measurements with “standard” interstellar dust limits any such effect. Compared to the Wind Model, radial exclusion around high mass galaxies has a stronger effect on large scale correlations, and the CDF shifts to somewhat higher values, though still too low to allow measurement of the CDF in the presence of quasar color variations.

We have also considered a “hybrid” model that uses the No-Wind simulation but includes reddening in galaxies with baryonic mass $M < 5.4 \times 10^{10} M_{\odot}$ (which dominates the intergalactic dust signal by a factor of 2 – 4) when computing the large scale galaxy-dust correlation. This model can reproduce the MSFR measurements with a physically acceptable dust-to-metal mass ratio of 0.39. However, while sightlines with $E(g-i) > 0.1$ are still rare in this model, they contribute a significant fraction of the mean reddening. Moreover, the galaxies presumed to produce most of the reddening in this model might well have detectable effects on quasar colors, visual morphologies, or spectra, and no such effects have been reported. Predictions for this model are also more sensitive to our mass and spatial resolution, and to the failure of the No-Wind simulation to match the low mass end of the observed galaxy baryonic mass function (Oppenheimer et al. 2010). In the end, we consider both the No-Wind and hybrid models to be illustrative demonstrations of how hard it is to reproduce the MSFR data *without* widespread galactic outflows.

The large scale galaxy-dust correlation measured by MSFR traces the shape of the galaxy-mass correlation function they infer from gravitational magnification, which in turn traces the known shape of the galaxy-galaxy correlation function. This large scale shape is almost inevitable in any model where the dust originates in galaxies, and we find it in all three of our models despite the very different spatial distributions of the dust. However, on sub-Mpc scales — the 1-halo regime — the detailed form of the correlation function has substantial diagnostic power for the sources of the dust, the extent and radial profile of outflows, and the survival of dust in these outflows, albeit in a combination that may be difficult to untangle. In this regime, our three models predict significantly different shapes, none of them in full agreement with the data, and the shape of the galaxy-metal correlations is quite different from the shape of the galaxy-gas correlations. Given the fairly large ($\sim 50\%$) observational error bars and our simplified modeling of MSFR’s angular measurements in terms of projected separations at an effective redshift, we have not attempted to use the detailed small-scale shape as a diagnostic or to assess the implications of moderate discrepancies with our theoretical predictions. However, future imaging surveys such as Pan-STARRS, the Dark Energy Survey, and LSST will provide much larger samples of quasars and foreground galaxies, allowing higher precision measurements in shells of photometric galaxy redshift. Over the past decade, galaxy-galaxy lensing has progressed from the first measurements of large scale galaxy-matter angular correlations (Fischer et al. 2000) to detailed measurements of projected mass correlations as a function of galaxy luminosity, color, morphology, and environment (McKay et al. 2001; Hoekstra et al. 2004; Sheldon et al. 2004; Mandelbaum et al. 2006). We anticipate similar progress in the studies of galaxy-dust correlations over the coming decade, providing new insights into the origin, evolution, and observational impact of solid-phase material in the intergalactic medium.

ACKNOWLEDGEMENTS

We thank Charlie Conroy, Bruce Draine, Brice Ménard, Ryan Scranton, Masataka Fukugita, and Gordon Richards for helpful discussions. We thank Vimal Simha for investigating the temperature distribution of wind particles as a function of halo mass (see §4). This work was supported in part by NSF Grant AST-0707985 and by an Ohio State University Fellowship to YZ. DW, MF, and DK gratefully acknowledge support from, respectively, an AMIAS membership at the IAS, the FCAD Fellows Program at the University of Massachusetts, and Harvard University.

REFERENCES

- Aguirre, A., Hernquist, L., Katz, N., Gardner, J., & Weinberg, D. 2001, *ApJL*, 556, L11
- Berlind, A. A., & Weinberg, D. H. 2002, *ApJ*, 575, 587
- Birnboim, Y., & Dekel, A. 2003, *MNRAS*, 345, 349
- Bovy, J., Hogg, D. W., & Moustakas, J. 2008, *ApJ*, 688, 198
- Blanton, M. R., et al. 2003, *ApJ*, 592, 819
- Chandrasekhar, S., Münch, G. 1952, *ApJ*, 115, 103
- Chelouche, D., Koester, B. P., & Bowen, D. V. 2007, *ApJL*, 671, L97
- Dekel, A., & Birnboim, Y. 2006, *MNRAS*, 368, 2
- Davé, R., Oppenheimer, B. D., & Sivanandam, S. 2008, *MNRAS*, 391, 110
- Draine, B. T. 2009, *Astronomical Society of the Pacific Conference Series*, 414, 453
- Draine, B. T., & Salpeter, E. E. 1979, *ApJ*, 231, 77
- Finlator, K., & Davé, R. 2008, *MNRAS*, 385, 2181
- Fischer, P., et al. 2000, *AJ*, 120, 1198
- Gingold, R. A., & Monaghan, J. J. 1977, *MNRAS*, 181, 375
- Hinshaw, G., et al. 2009, *ApJs*, 180, 225
- Hoekstra, H., Yee, H. K. C., & Gladders, M. D. 2004, *ApJ*, 606, 67
- Issa, M. R., MacLaren, I., & Wolfendale, A. W. 1990, *A&A*, 236, 237
- Kaneda, H., Yamagishi, M., Suzuki, T., & Onaka, T. 2009, *ApJL*, 698, L125
- Kereš, D., Katz, N., Fardal, M., Davé, R., & Weinberg, D. H. 2009a, *MNRAS*, 395, 160
- Kereš, D., Katz, N., Davé, R., Fardal, M., & Weinberg, D. H. 2009b, *MNRAS*, 396, 2332
- Kereš, D., Katz, N., Weinberg, D. H., & Davé, R. 2005, *MNRAS*, 363, 2
- Lisenfeld, U., & Ferrara, A. 1998, *ApJ*, 496, 145
- Lucy, L. B. 1977, *AJ*, 82, 1013
- McKay, T. A., et al. 2001, preprint (astro-ph/0108013)
- Mandelbaum, R., Seljak, U., Kauffmann, G., Hirata, C. M., & Brinkmann, J. 2006, *MNRAS*, 368, 715
- McGee, S. L., & Balogh, M. L. 2010, *MNRAS*, 405, 2069
- Ménard, B., Nestor, D., Turnshek, D., Quider, A., Richards, G., Chelouche, D., & Rao, S. 2008, *MNRAS*, 385, 1053
- Ménard, B., Scranton, R., Fukugita, M., & Richards, G. 2010, *MNRAS*, 405, 1025 (MSFR)
- Ménard, B., Kilbinger, M., & Scranton, R. 2010, *MNRAS*, 406, 1815
- Muller, S., Wu, S.-Y., Hsieh, B.-C., González, R. A., Loinard, L., Yee, H. K. C., & Gladders, M. D. 2008, *ApJ*, 680, 975
- Murray, N., Quataert, E., & Thompson, T. A. 2005, *ApJ*, 618, 569
- Gnedin, N. Y., & Ostriker, J. P. 1997, *ApJ*, 486, 581

- Oppenheimer, B. D., & Davé, R. 2006, MNRAS, 373, 1265
 Oppenheimer, B. D., & Davé, R. 2008, MNRAS, 387, 577
 Oppenheimer, B. D., & Davé, R. 2009, MNRAS, 395, 1875
 Oppenheimer, B. D., Davé, R., Kereš, D., Fardal, M., Katz, N.,
 Kollmeier, J. A., & Weinberg, D. H. 2010, MNRAS, 406, 2325
 Ostriker, J. P., & Heisler, J. 1984, ApJ, 278, 1
 Peacock, J. A., & Smith, R. E. 2000, MNRAS, 318, 1144
 Richards, G. T., et al. 2004, ApJs, 155, 257
 Sheldon, E. S., et al. 2004, AJ, 127, 2544
 Springel, V. 2005, MNRAS, 364, 1105
 Tremonti, C. A., et al. 2004, ApJ, 613, 898
 van der Marel, R. P., Alves, D. R., Hardy, E., & Suntzeff, N. B.
 2002, AJ, 124, 2639
 York, D. G., et al. 2000, AJ, 120, 1579
 Zaritsky, D. 1994, AJ, 108, 1619
 Zwicky, F. 1962, in IAU Symp. 15, Problems of Extragalactic Re-
 search, ed. G. C. McVittie (New York: Macmillan), 347